http://eprints.gla.ac.uk/170339/

Deposited on 03 October 2018

Angle of attack dependence of flow past cactus-inspired cylinders with a low number of ribs

Oleksandr Zhdanov[a,*], Angela Busse[a]

[a]*School of Engineering, University of Glasgow, Glasgow G12 8QQ, United Kingdom*

Abstract

The aerodynamic coefficients and the Strouhal number of cylinders with three and four ribs, inspired by succulents *Euphorbia trigona* and *Euphorbia Abyssinica* are investigated using 2D Unsteady Reynolds-Averaged Navier-Stokes simulations at Reynolds number 20,000. Both configurations show a significant dependence of the studied characteristics on the angle of attack. The obtained results are compared to the smooth circular cylinder, previous results for cylinders with 24 ribs based on the Saguaro cactus, and cylinders with triangular and square cross-sections. Relative to the circular cylinder, the mean drag coefficient is lowered only for the four-rib case at high angles of attack. However, at some angular positions, the ability to reduce unsteady force fluctuations exceeds Saguaro-inspired cylinders. For both shapes studied, the Strouhal number at most angles of attack is lower compared to both the circular cylinder and cylinders with 24 ribs at the same Reynolds number. The minimum values of the aerodynamic coefficients for both configurations are related to the angular orientation. For the four-rib case a critical angle of $\alpha_{cr} \approx 40°$ is observed, at which the mean drag coefficient and the fluctuating lift coefficient attain their minima. The mean lift coefficient reaches at this angle its maximum value before a sudden drop for higher angles of attack. Therefore, for cactus-shaped cylinders with four ribs high angles of attack give the optimum orientation relative to prevailing winds.

Keywords: Cactus-inspired cylinder, Bluff bodies, Aerodynamic coefficients, Strouhal number

1. Introduction

The shape and structural features of cacti have significant importance for their survival in the natural environment. For example, ribs and spines play a vital role in fog collection (Ju et al., 2012) and control of moisture evaporation

---

*Corresponding author
 E-mail address:* `o.zhdanov.1@research.gla.ac.uk` (Oleksandr Zhdanov)

from the surface of the plants. Moreover, ribs and cavities have another function, as they can help to decrease wind loads and to prevent wind damage and uprooting by modifying the flow field around the plant.

In terms of aerodynamics, cacti are classified as bluff-bodies that resemble cylinders with ribs. Research on flow past cylindrical type structures has wide engineering applications to buildings, structural elements, risers, cables, etc. A widely studied grooved cylinder shape, investigated first by Talley et al. (2001), is a biomimetic shape based on the cross-section of the Saguaro cactus. Originating from the deserts of the South-West of the United States and the Mexican State of Sonora, these tall, tree-like and ribbed (10 to 30 ribs) plants have the ability to withstand high winds without being broken or uprooted, despite having only a shallow root system (Pierson and Turner, 1998).

Talley et al. (2001) and Talley and Mungal (2002) conducted numerical and experimental studies using Saguaro-like cylinders with 24 V-shaped ribs at Reynolds numbers of 20,000 up to 100,000. They found a reduction of the mean drag coefficient, lower lift and drag force fluctuations and an increase in the Strouhal number compared to the smooth cylinder.

Extensive experimental and numerical research by Liu and co-authors (Liu et al., 2011; Wang et al., 2014; Jie and Liu, 2016) on the 24 V-shaped grooves cactus cylinder configuration also confirmed the previous observations in terms of the ability of ribbed cylinders to damp fluctuations of longitudinal (up to 50%) and cross-flow unsteady forces at low (Liu et al., 2011) and high (Wang et al., 2014; Jie and Liu, 2016) Reynolds numbers. The visualisations by Liu et al. (2011) showed small recirculation flows within the cavities of the grooved cylinder, similar to those discovered previously by Babu and Mahesh (2008). The presence of these vortices was also demonstrated experimentally (Wang et al., 2014) and numerically (Jie and Liu, 2016) at a higher Reynolds number of 54,000.

Recent experiments by Letchford et al. (2016) on cactus-shaped cylinders placed in smooth and rough boundary layers at Reynolds numbers from 10,000 to 20,000 showed the reduction of the aerodynamic coefficients and an increase in the Strouhal number, which is consistent with the two-dimensional results by Talley et al. (2001). This indicates that the results from previous studies for the two-dimensional case also translate to three-dimensional structures. In addition, the dependence of the cactus orientation with respect to the flow direction was reported to show little variation.

The studies discussed above are all focused on the 'classical' ribbed cylinder configuration with 24 V-shaped grooves introduced by Talley et al. (2001). The effect of the number and the shape of grooves was first studied by Yamagishi and Oki (2004, 2005) for Reynolds numbers ranging from 10,000 to 400,000 using experiments and numerical simulations. Both cylinders with U- and V-shaped grooves yielded significant reduction in drag compared to the smooth cylinder, but drag reduction for cylinders with V-shaped grooves was found to be up to 15% higher than for cylinders with U-shaped grooves. The critical Reynolds number was found to decrease with increasing number of grooves.

Zhou et al. (2015) experimentally determined aerodynamic properties of the

Figure 1: *Euphorbia trigona*, a member of the Euphorbiaceae family, in Glasgow Botanic Gardens.

cylinders with 16 rectangular grooves in the Reynolds number range from 7,400 to 18,000. As in the case of other groove shapes, significant drag reduction was found together with the property of the grooved cylinder to mitigate vortex shedding.

The lowest number of ribs investigated so far has been the configuration used by Abboud et al. (2011) and El-Makdah and Oweis (2013), a cylinder with eight U-shaped grooves. Visualisation of the flow (El-Makdah and Oweis, 2013) near the cactus surface showed the presence of counter-rotating vortices, similar to those discovered numerically by Babu and Mahesh (2008). The authors suggest that there may be significant dependence of the flow field on the angle of attack for cacti with a low number of ribs, but they give results only for an angle of attack of zero degrees.

As discussed above, most studies on the aerodynamic characteristics and flow around cacti have focussed on cactus-shaped cylinders with many grooves, a shape inspired by the Saguaro cactus. However, a number of cacti have only three or four ribs, e.g., *Cereus*, *Trichocereus pachanoi*, and *Calymmanthium*. Moreover, a number of succulents from the Euphorbiaceae family (figure 1) from the Eastern Hemisphere, which in the process of convergent evolution developed a similar plant structure, including ribs and spines, as members of the Cactaceae family in the Western Hemisphere (McGhee, 2011), have only a low number of ribs (e.g. *Euphorbia trigona*, *Euphorbia Abyssinica*). Considering similar wind conditions in their natural environment, succulents may have similar aerodynamic benefits from their shape as the Saguaro cactus.
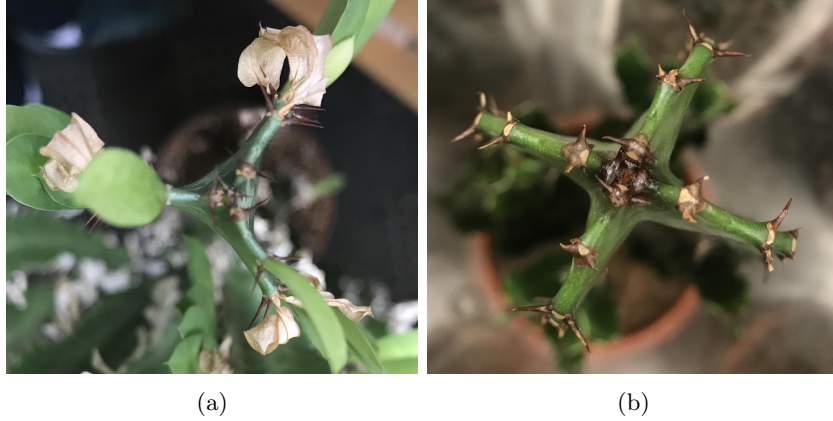
3

(a)   (b)

Figure 2: Succulents with low number of ribs: a - *Euphorbia trigona*, b - *Euphorbia Abyssinica*.

The present study focusses on the flow past cylinders with a low number of ribs based on the succulents *Euphorbia trigona* and *Euphorbia Abyssinica* at the biologically relevant Reynolds number of about 20,000. The goal is to establish whether the shapes adopted by these succulents have similar aerodynamic features as the Saguaro cactus. Unlike the cactus-shaped cylinders with many ribs in most of previous studies, the aerodynamic characteristics of cacti with a low number of ribs should be strongly dependent on the angle of attack (El-Makdah and Oweis, 2013).

In the present work, the dependence of the aerodynamic coefficients and Strouhal number on the angle of attack is studied numerically. The investigated shapes, a three-rib and a four-rib cylinder, are described in section 2, and the numerical methodology is discussed in section 3. In sections 4.1 to 4.3 the dependence of the aerodynamic coefficients and of the Strouhal number on the angle of attack are discussed for both investigated geometries. The influence of the projected frontal width is discussed in section 4.4, where the force coefficients and the Strouhal number of the four-rib and three-rib cactus-shaped cylinders are also compared to results for square cylinders and triangular prisms. In section 4.5 flow visualisations are employed to gain insight into the angle of attack dependence of the mean flow fields. In the last section general conclusions are given.

2. Investigated geometries

Following the approach of previous work on cacti with many ribs (Talley et al., 2001; Talley and Mungal, 2002), we approximate the shape of *Euphorbia Trigona* (figure 2a) and *Euphorbia Abyssinica* (figure 2b) using two-dimensional configurations where the cross-section shape is described using simple geometrical relations (see figure 3). The equivalent circle of diameter D was divided into three or four parts by an equilateral triangle or square depending on the configuration. At the intersection points with the circle, ribs with minimum
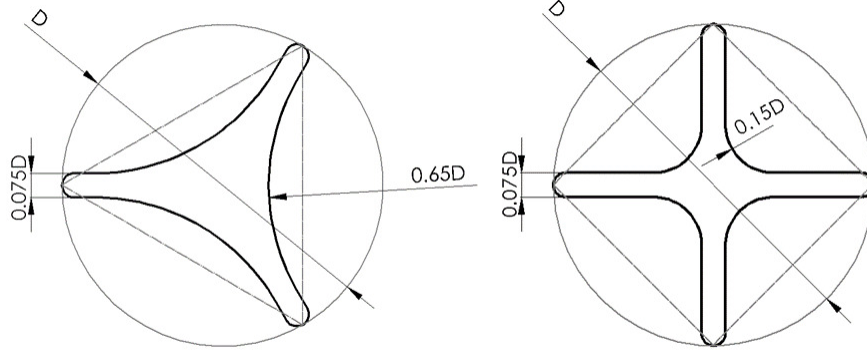
4

Figure 3: Geometrical representation of the tested cactus shapes. Left: three-rib configuration approximating *Euphorbia trigona*; right: four-rib configuration approximating *Euphorbia Abyssinica*.

thickness of $0.075D$ and tip radius of half of the thickness were constructed. The grooves between ribs correspond to approximate representations of cross-sections of *Euphorbia Trigona* and *Euphorbia Abyssinica*. In the three-rib case the grooves are formed by conjugating ribs with the fillets of radius $0.65D$ while the four-rib case has fillets of $0.15D$ between neighbouring ribs. We will refer to these shapes as 'cactus-shaped cylinders' in the following, even though *Euphorbia trigona* and *Euphorbia Abyssinica* are not members of the Cactaceae family, i.e., they are succulents and not cacti in the botanical classification.

In the following, numerical simulations will be used to investigate the flow past the described three-rib and four-rib cylinders at a Reynolds number of $20,000$. For example, for a succulent stem of diameter $D = 0.08$ m this would correspond to a wind speed of ≈ 4 m/s in dry air at 27 °C . This velocity falls into the range of mean summer wind speed measured in the natural environment of succulents (Teboho et al., 2017).

3. Numerical method

As in the studies by Yamagishi and Oki (2004, 2005) and Talley et al. (2001) in the present study unsteady Reynolds-Averaged Navier-Stokes (URANS) simulations are used. The CFD solver Star-CCM+ v11.04 by Siemens PLM Software (Siemens, 2017) was employed. For the spatial discretisation a second order accurate finite volume discretisation with second order upwind scheme for the convective flux was used; a second order implicit scheme was selected for the discretisation in time. The Spalart-Allmaras turbulence model was used in combination with a low y^+ approach. This is known to give satisfactory results for the smooth cylinder case (Apaçoğlu and Aradağ, 2011).

The computational domain is shown in Figure 4. The size of the domain is $32.5D$ in the streamwise direction leaving $20D$ behind the cylinder. In the cross-stream direction, the computational domain has an extent of $25D$. Benim
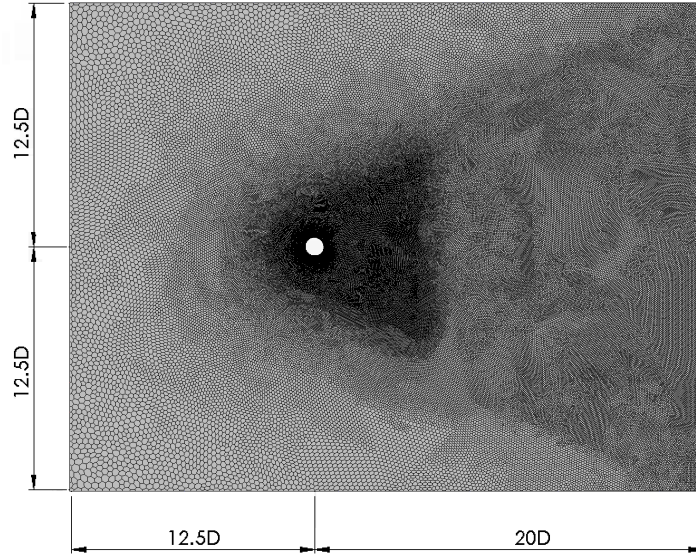
Figure 4: Computational domain with grid used for the simulations

et al. (2008) found that blockage effects of a cylinder become negligible for $H/D > 6$, where H is half of the domain size in the cross-stream direction for Reynolds-Averaged Navier-Stockes (RANS) simulations. In this study $H/D = 12.5$, so blockage effects are expected to be very low. This was confirmed by a simulation with doubled domain size in streamwise and cross-stream direction for the smooth cylinder case ($H/D = 25$), which showed negligible influence of the domain size effect on the drag and lift coefficients (Table 1).

An unstructured mesh consisting of polyangular cells was used for the discretisation of the domain (see figure 4). The use of polyangular cells allows the construction of meshes with low cell skewness (Siemens, 2017) for the cactus-shaped cylinder cases. The mesh was refined close to the cylinder and in the wake of the cylinder. Prismatic cells were placed on solid boundaries, i.e. on the surface of the cylinder, for improved resolution of the near wall flow (figure 5). The prismatic layers were stretched with a geometric stretching factor of 1.11, yielding wall y^+ values < 1 at the solid boundaries and gradually increasing in size to match the size of the polyangular cells close to the cylinder. The typical number of cells used for the simulations is $\approx 110,000$ for the circular cylinder, $\approx 180,000$ for the three-rib cases, and $\approx 310,000$ for the four-rib cases.

The inlet was placed at the left side of the computational domain, and a uniform inlet velocity of U_∞ was applied at this boundary. Standard pressure outlet conditions were applied on the outlet of the domain. Symmetry boundary conditions were applied at the top and bottom boundaries of the computational domain.

The Reynolds number of the flow, based on free-stream velocity U_∞ and outer diameter D was set at 20,000. This, biologically relevant, Reynolds num-
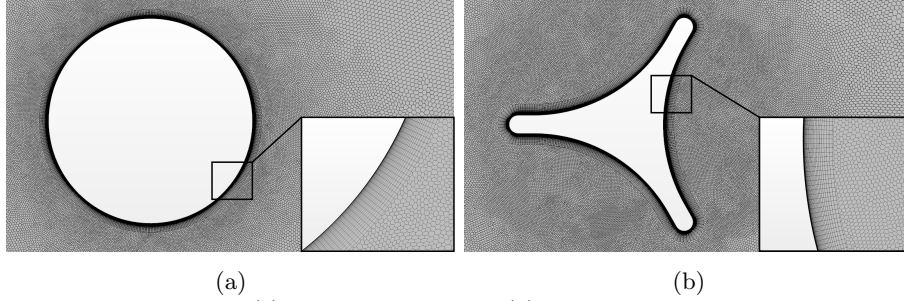
6

Figure 5: Mesh close to (a) circular cylinder and (b) three-rib cactus-shaped cylinder with enlarged prism layers.

ber has already been used in a number of studies related to the Saguaro cactus (Talley et al., 2001; Talley and Mungal, 2002; Letchford et al., 2016). A non-dimensional time step of $\Delta t U_\infty / D = 7.833 \times 10^{-3}$ was used for the numerical simulations. Results were extracted once the unsteady force coefficient fluctuations settled down to a quasi-stationary pattern and the amplitude of the oscillations had attained constant values.

The computational approach was validated using the standard smooth cylinder due to the wealth of experimental and numerical data available for this case. The results for the mean drag coefficient C_d, rms lift coefficient C_l', amplitude of the lift coefficient fluctuations C_l^{amp}, and Strouhal number St show overall good agreement with numerical and experimental studies (Table 1). All measured values are very close to the results of Apaçoğlu and Aradağ (2011) who used the same turbulence model. A comparison with the data by Talley et al. (2001), who used the $v^2 - f$ turbulence model, shows that the Spalart-Allmaras turbulence model gives overall a better match to experiments and LES. The determined magnitude of the drag coefficient is close to experimental studies conducted at the same Re (West and Apelt, 1993; Lim and Lee, 2002). The computed value of the rms lift coefficient is consistent with the LES results by Lysenko et al. (2014), but exceeds the experimental values of Norberg (2003) and West and Apelt (1993). However, even experimental results (Table 1) for these two parameters show a significant scatter. As discussed by West and Apelt (1993) and Lysenko et al. (2014) this is due to a number of factors such as cylinder surface roughness, blockage ratio, free stream turbulence, cylinder span, etc., which can affect experimental data.

4. Results and discussion

The investigated cactus-shaped cylinders have 3-fold rotational symmetry (three-rib configuration) or 4-fold rotational symmetry (four-rib configuration). Dependence of their flow properties on the angle of attack (α) (see figure 6) was tested for the three-rib configuration in the range from 0° to 60° in 5° steps, while for the four-rib configuration the angle of attack was varied from 0° to 45° in 3.75° steps. In order to determine the angle of attack at which

Table 1: Overview of the experimental and numerical values of the aerodynamic coefficients and Strouhal number for circular cylinder at Re = 20,000. Entries for the rms lift coefficient C'_l marked with * have been computed from the amplitude of the lift fluctuations C_l^{amp} assuming a sinusoidal signal.

|	Method	C_l^{amp}	C'_l	C_d	St
Current simulation H/D = 12.5	URANS	1.12	0.80	1.17	0.228
Current simulation H/D = 25	URANS	1.12	0.79	1.15	0.225
Apaçoğlu and Aradağ (2011)	URANS	1.1	$(0.78)^*$	1.17	0.22
Norberg (2003)	Experiment	-	0.47	-	0.194
Lysenko et al. (2014)	LES	-	$0.61 - 0.75$	$1.30 - 1.39$	$0.17 - 0.20$
West and Apelt (1993)	Experiment	-	$0.49 - 0.68$	$1.14 - 1.4$	0.195
Lim and Lee (2002)	Experiment	-	-	1.2	0.187
Talley et al. (2001)	URANS	1.923	$(1.360)^*$	1.683 ± 0.164	0.217
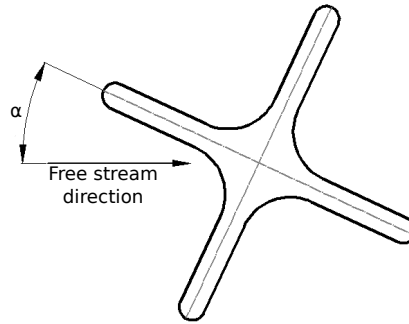
Figure 6: Angle of attack definition for the cactus-shaped cylinder.

the drag force coefficient attains its minimum, additional simulations were performed with smaller steps in the corresponding angle of attack ranges. The $\alpha = 0°$ configuration corresponds to the orientation where the rib at the windward side of the cactus is aligned with the direction of free-stream velocity. At 60° (three-rib configuration) and 45° (four-rib configuration) angle of attack the groove/cavity between ribs faces the free-stream flow. Due to the mirror symmetry of the studied configurations with respect to any rib axis, higher angles of attack ranging from 60° to 120° (three-rib configuration) or 45° to 90° (four-rib configuration) will give the same absolute values of the aerodynamic coefficients as the corresponding configuration at angle of attack $(120° - \alpha)$ or $(90° - \alpha)$ respectively. Therefore, in the following results will be shown as a function of $\alpha/\alpha_{\mathrm{max}}$, where $\alpha_{\mathrm{max}} = 60°$ for the three-rib case and $\alpha_{\mathrm{max}} = 45°$ for the four-rib case.

The force coefficients were calculated during the simulations as

$$C_{d,l} = \frac{\overline{f_{x,y}}}{\frac{1}{2}\rho U_\infty^2 D} \tag{1}$$

$$C'_{d,l} = \frac{\sigma(f_{x,y})}{\frac{1}{2}\rho U_\infty^2 D}, \tag{2}$$

where $\overline{f_{x,y}}$ is the mean value of the force in the respective direction (x for the drag and y for the lift), $\sigma(f_{x,y})$ the root mean square deviation of $f_{x,y}$, and D the equivalent circle diameter. As expected, the aerodynamic coefficients and the Strouhal number exhibit a strong dependence on the angle of attack for both the three-rib and the four-rib configuration.

4.1. Drag coefficient

The dependence of the mean drag coefficient, C_d, on the angle of attack is shown in figure 7. In both cases C_d shows strong variations with angle of attack. In the three-rib case, C_d attains its lowest values close to an intermediate angle of attack at $\alpha = 27.5°$ ($\alpha/\alpha_{\mathrm{max}} \approx 0.46$)and its maximum values for 0° and 50° ($\alpha/\alpha_{\mathrm{max}} \approx 0.83$). A difference of over 60% was found between the maximum and the minimum values of the drag coefficient. Compared to the smooth cylinder case, the C_d value is increased for all angles of attack for the three-rib configuration.

In contrast, the C_d values of the four-rib configuration are lower than the value for the smooth cylinder case at high angles of attack $\alpha > 36°$($\alpha/\alpha_{\mathrm{max}} > 0.8$). As the angle of attack is decreased for this configuration, the value of C_d increases, and C_d attains its maximum value for $\alpha = 0$. The maximum value of C_d is more than double compared to the C_d value for the circular cylinder case and also exceeds the maximum values observed for the three-rib configuration.

Unlike in previous studies on cactus-shaped cylinders with many ribs (Talley et al., 2001; Yamagishi and Oki, 2004, 2005; Letchford et al., 2016) significant drag reduction compared to the circular cylinder was not observed in the present study. However, the four ribbed configuration showed between $\alpha = 36°$
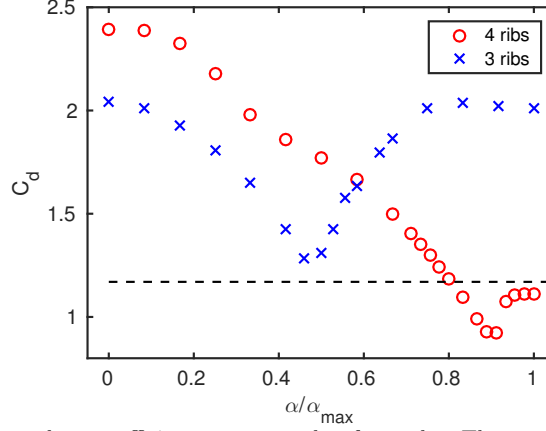
9

Figure 7: Mean drag coefficient versus angle of attack. The angle of attack has been normalised with the maximum angle of attack (three-rib case: $\alpha_{\max} = 60°$, four-rib case: $\alpha_{\max} = 45°$). The dashed line indicates the value for the smooth circular cylinder case.

($\alpha/\alpha_{\max} = 0.8$) and 45° ($\alpha/\alpha_{\max} = 1$) C_d values below the value for a smooth circular cylinder.

In order to assess the fluctuations in the streamwise force, root mean square (rms) values of the fluctuating part of the drag coefficient C_d' were determined for both cactus shapes (see figure 8). Like the mean drag coefficient, C_d' shows significant variation as the angle of attack is changed. For both the three-rib and the four-rib configuration C_d' attains its minimum value at $\alpha_{\max}$, i.e. for the orientation where a cavity is centred at the windward side of the cactus. For the three-rib case the C_d' value at $\alpha_{\max}$ is close to the value for the smooth cylinder case. In contrast, a substantial reduction in C_d' compared to the smooth cylinder case is observed for the four-rib case at $\alpha > 39°$ ($\alpha/\alpha_{\max} > 0.86$). At lower angles of attack, C_d' is significantly higher than in the smooth cylinder case for both the three-rib and the four-rib configuration, and no simple dependence on the angle of attack can be observed. Moreover, a sudden increase in C_d' is observed between $\alpha = 27.5°$ ($\alpha/\alpha_{\max} \approx 0.46$) and $\alpha = 40°$ ($\alpha/\alpha_{\max} \approx 0.66$) in the three-rib case. For cactus configurations with many ribs reduction in the unsteady drag forces was found by Talley et al. (2001), Letchford et al. (2016) for the same Reynolds number and by Babu and Mahesh (2008) for the laminar regime. In the current study, a significant reduction is observed only for the four-rib configuration at high angles of attack. Taking into account the behaviour of the C_d and C_d' it can be conjectured that stems of succulents and cacti may be orientated with respect to the prevailing winds in the natural environment in a way to minimise their wind loading as they grow.

4.2. Lift coefficient

Figure 9 shows the variation of the mean lift coefficient C_l with angle of attack. For angles of attack where symmetry with respect to the mean flow
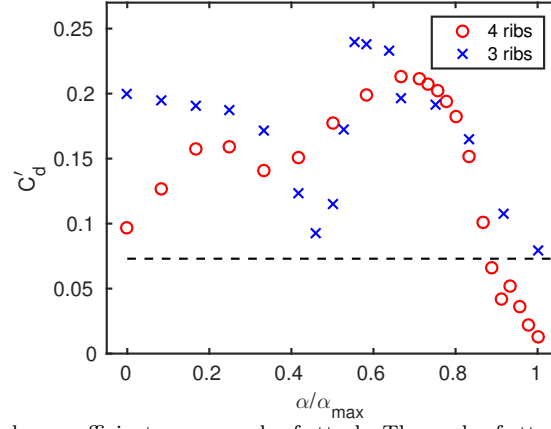
Figure 8: Rms drag coefficient versus angle of attack. The angle of attack has been normalised with the maximum angle of attack (three-rib case: $\alpha_{\max} = 60°$, four-rib case: $\alpha_{\max} = 45°$). The dashed line shows the value for the smooth cylinder case.
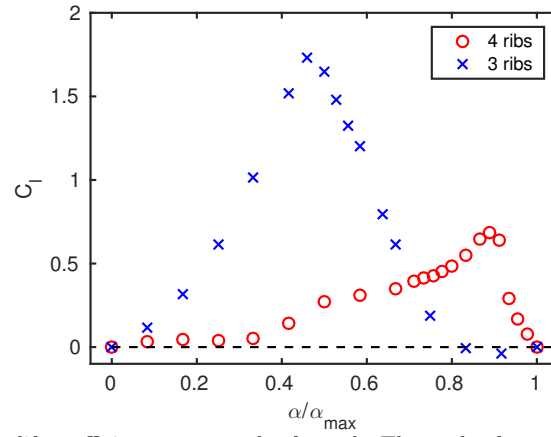

Figure 9: Mean lift coefficient versus angle of attack. The angle of attack has been normalised with the maximum angle of attack (three-rib case: $\alpha_{\max} = 60°$, four-rib case: $\alpha_{\max} = 45°$). The dashed line shows the value for the smooth cylinder case.

11

direction is given, a zero mean lift coefficient is found, as expected. Thus at zero and maximum angle of attack the mean lift coefficient is zero. At all other angles of attack, symmetry with respect to the mean flow direction is not preserved, and we therefore expect non-zero values for the lift coefficient.

The change of the mean lift coefficient with the angle of attack in the three-rib case demonstrates an opposite trend to the mean drag coefficient for the same configuration. The maximum value of C_l is attained close to an intermediate angle of attack ($\alpha = 27.5°$) ($\alpha/\alpha_{\max} \approx 0.46$), while minimum values occur for $\alpha = 0°$ and $\alpha_{\max}$. Compared to the drag coefficient, the lift coefficient shows a stronger variation with angle of attack for the three-rib configuration.

For the four-rib configuration, the maximum mean lift coefficient is attained for $\alpha = 40°$ ($\alpha/\alpha_{\max} \approx 0.89$), but its value is still more than two times lower compared to the maximum value in the three-rib case. The maximum value of C_l is followed by a sudden drop. In general, the four-rib case demonstrates a lower dependence of C_l on the angle of attack.

Most previous studies on flow past cactus-shaped cylinders with many ribs did not report on angle of attack dependence (Talley et al., 2001; Yamagishi and Oki, 2004, 2005; Liu et al., 2011; Wang et al., 2014; Jie and Liu, 2016) or stated that the influence of the angular position is insignificant (Letchford et al., 2016). Oweis et al. (2011, 2013), who studied the flow around a cactus-shaped cylinder with eight ribs, pointed out that a change in the angular position will have an effect on the flow characteristics. However, they did not investigate the angle of attack dependence for their configuration.

In the current study, a decrease in angle of attack dependence was found when proceeding from a three-rib to a four-rib configuration. We expect that this trend will continue as the number of ribs of a cactus is increased, since with increasing number of ribs the range of possible different angular orientations decreases and the configuration approaches a more circular shape. Thus the angle of attack dependence of the mean lift coefficient should be lower but still noticeable for a cylinder with eight ribs compared to the current configurations, and attain negligible variation with angle of attack, i.e. approach $C_l = 0$, for the classical cactus configuration with 24 ribs.

The rms value of the fluctuating part of the lift coefficient, C_l', is shown in figure 10. For most angles of attack, the rms lift coefficient is reduced compared to the smooth cylinder. The cactus-shaped cylinders demonstrate opposite trends in C_l' behaviour with angle of attack for the three- and the four-rib configuration. For the three-rib configuration, C_l' increases with angle of attack, whereas the four-rib configuration shows a decrease of C_l' with increasing angle of attack up to $\alpha = 41°$ ($\alpha/\alpha_{\max} \approx 0.91$) followed by slight increase towards $\alpha_{\max}$. The lift force fluctuations are reduced by up to 85% compared to the smooth cylinder case in the range of angles of attack ranging from $\alpha = 0°$ to $\alpha = 45°$ ($\alpha/\alpha_{\max} = 0.75$) for the three-rib case. The four-rib configuration also shows reduction of the lift force fluctuations. This effect starts from $\alpha = 15°$ ($\alpha/\alpha_{\max} \approx 0.33$) and increases with angle of attack reaching 77% reduction compared to the smooth cylinder case at $\alpha = 41°$ ($\alpha/\alpha_{\max} \approx 0.91$). The results for C_l' are consistent with the observation that have been made for cylinder with
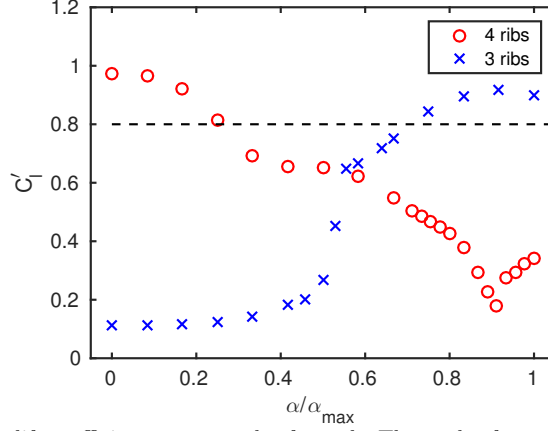
Figure 10: Rms lift coefficient versus angle of attack. The angle of attack has been normalised with the maximum angle of attack (three-rib case: $\alpha_{\max} = 60°$, four-rib case: $\alpha_{\max} = 45°$). The dashed line shows the value for the smooth cylinder case.

many ribs (Talley et al., 2001; Babu and Mahesh, 2008; Wang et al., 2014; Jie and Liu, 2016; Letchford et al., 2016) in terms of the ability of cactus-shaped cylinders to mitigate unsteady lift force fluctuations. The maximum decrease in C'_l observed in the current study is higher than in other works where the maximum reduction reported by Wang et al. (2014) and Jie and Liu (2016) was 50%.

Representative sections of the time histories of the lift force fluctuations are shown in figure 11. As expected, a clear periodic behaviour can be observed in all cases. Some higher frequency content can be observed, which is stronger for the three-rib cylinder at low angle of attack. A similar observation has been made in the experiments by Nakagawa (1989), who showed that pressure fluctuations around a triangular prism have a more regular pattern at $\alpha = 60°$ compared to $\alpha = 0°$. This is consistent with the present results for the three-rib case. The angle of attack dependency of the lift force coefficient support the conjecture that the plant can minimise the possibility of wind damage by orientating itself with the prevailing wind direction. This is discussed in more detail in section 4.5.

4.3. Strouhal number

The Strouhal number (figure 12) was determined using Fast Fourier Transformation of the lift coefficient fluctuation as a function of time. Following the approach for the force coefficients calculation, the equivalent circle diameter was used as the characteristic length for St. Cactus-shaped cylinders of both configurations yield lower Strouhal numbers compared to the smooth cylinder over the whole range of angle of attack, except for the three-rib case between $\alpha = 20°$ ($\alpha/\alpha_{\max} \approx 0.33$) and $\alpha \approx 27.5°$ ($\alpha/\alpha_{\max} \approx 0.46$). In the four-rib case a maximum decrease of 25% in Strouhal number occurs at $\alpha_{\max}$, while in the
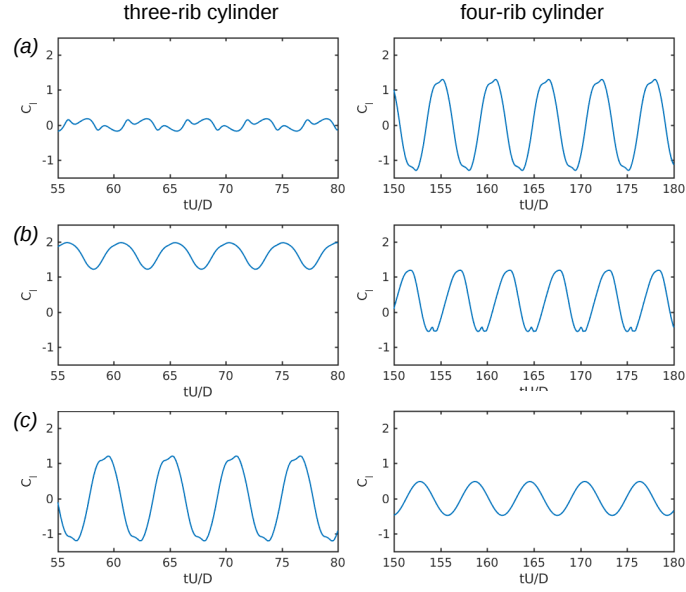
Figure 11: Time history of C_l for three- and four-rib cylinders at angles of attack normalised with maximum angle of attack: (a) - $\alpha/\alpha_{\max} = 0$, (b) - $\alpha/\alpha_{\max} = 0.5$, (c) - $\alpha/\alpha_{\max} = 1$.
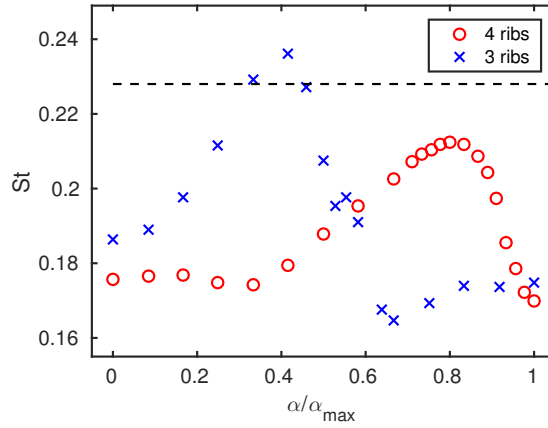

Figure 12: Strouhal number versus angle of attack. The angle of attack has been normalised with the maximum angle of attack (three-rib case: $\alpha_{\max} = 60°$, four-rib case: $\alpha_{\max} = 45°$). The dashed line shows the value for the smooth cylinder case.

14

three-rib case the lowest value is observed at $\alpha = 40°$ ($\alpha/\alpha_{\max} \approx 0.67$). At this angle of attack St is 28% lower compared to the circular cylinder. Babu and Mahesh (2008) observed a decrease in Strouhal number by 6.25% and 10.6% for flow past cylinders with many ribs in the laminar regime. However, it is difficult to relate their findings to the current results as the present study was performed in the turbulent flow regime and at a considerably higher Reynolds number. Previous experimental (Letchford et al., 2016) and numerical (Talley et al., 2001) results for the same Reynolds number (20,000), as used in this study, showed an increase of St for a classical ribbed cylinder compared to the smooth cylinder case.

4.4. Influence of the projected frontal width

Whereas for a smooth, circular cylinder the cylinder diameter is the obvious choice for the characteristic linear dimension in the computation of aerodynamic coefficients and Strouhal number, in the case of non-circular two-dimensional cross-sections there are several possible choices for the characteristic linear dimension. For example, in the context of square and equilateral triangular cylinders both the side of the square/triangle or its projected width are in wide use as characteristic linear dimension. The projected width of a non-circular object will change with angle of attack, and therefore the angle of attack dependence of its aerodynamic coefficients will be influenced by the choice of the characteristic linear dimension.

In the following, the current results are revisited using the projected frontal width D^* instead of the equivalent circle diameter as characteristic linear dimension and then compared to the angle of attack dependence of the force coefficients of similar bluff bodies, i.e. square cylinders and equilateral triangular prisms. The projected frontal widths were based on the inscribed triangle and square (see Figure 3) used in their construction. This gives for the three-rib case

$$D^* = \frac{\sqrt{3}D}{2}\cos(|\alpha - 30°| - 30°),\tag{3}$$

and for the four-rib case

$$D^* = D\cos(\alpha).\tag{4}$$

Force-coefficients and Strouhal numbers that have been computed with the projected frontal width as a characteristic dimension are marked with asterisks, e.g., C_d^* and St^*, to distinguish them from the results discussed in the previous sections.

As expected substitution of the projected frontal width instead of the equivalent circle diameter increased the values of the force coefficients at all angles attack except $\alpha = 0°$ for the four-rib case, where the projected frontal width is equal to the diameter $D = D^*$, and at angles of attack where the value of the force coefficients is 0 in both studied configurations (see figure 13 and 14). The values of C_d^* in the four-rib case exceed those for the circular cylinder at all angles of attack, but are close to it at $\alpha \approx 40°$. The decreased values of
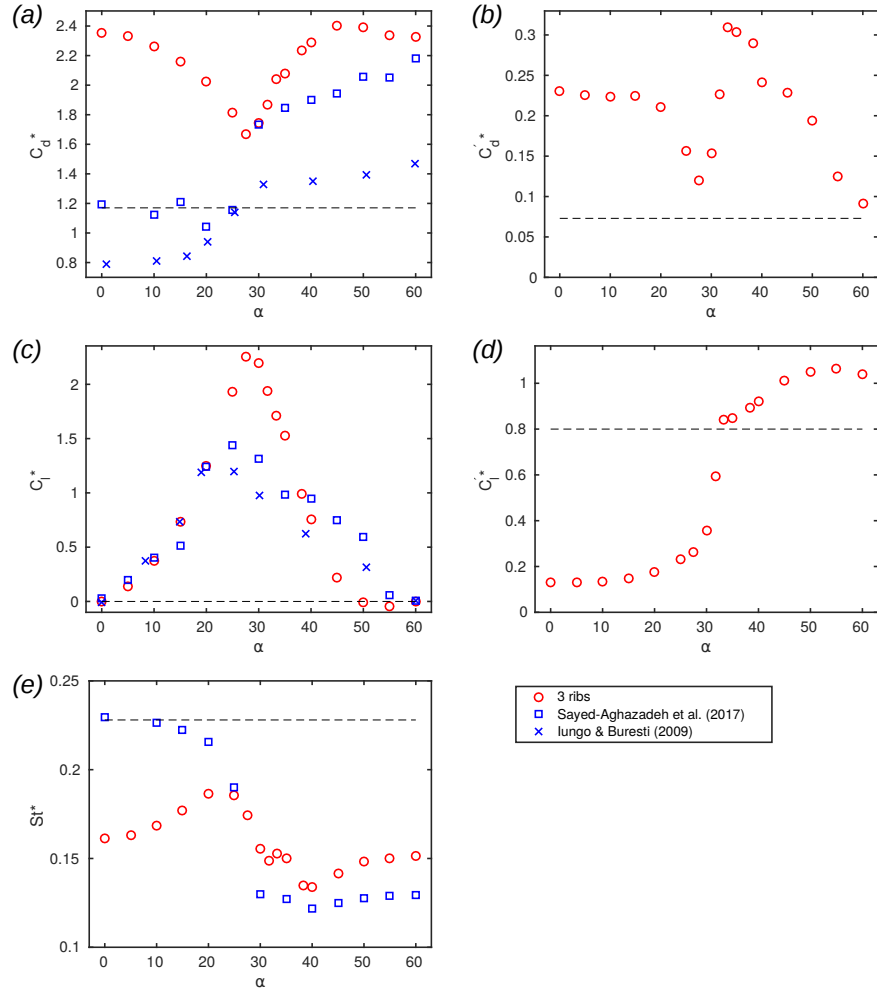
15

Figure 13: Mean and fluctuating lift force coefficients and Strouhal number calculated using projected frontal width as characteristic linear dimension versus angle of attack for the three-rib case and triangular prism: a) C_d^*, b) $C_d'^*$, c) C_l^*, d) $C_l'^*$, e) St^*. The dashed line shows the value for the smooth cylinder case. Data from experimental studies for low-aspect ratio triangular cylinders Iungo and Buresti (2009) and high-aspect ratio cylinders Seyed-Aghazadeh et al. (2017) are shown for comparison where available.
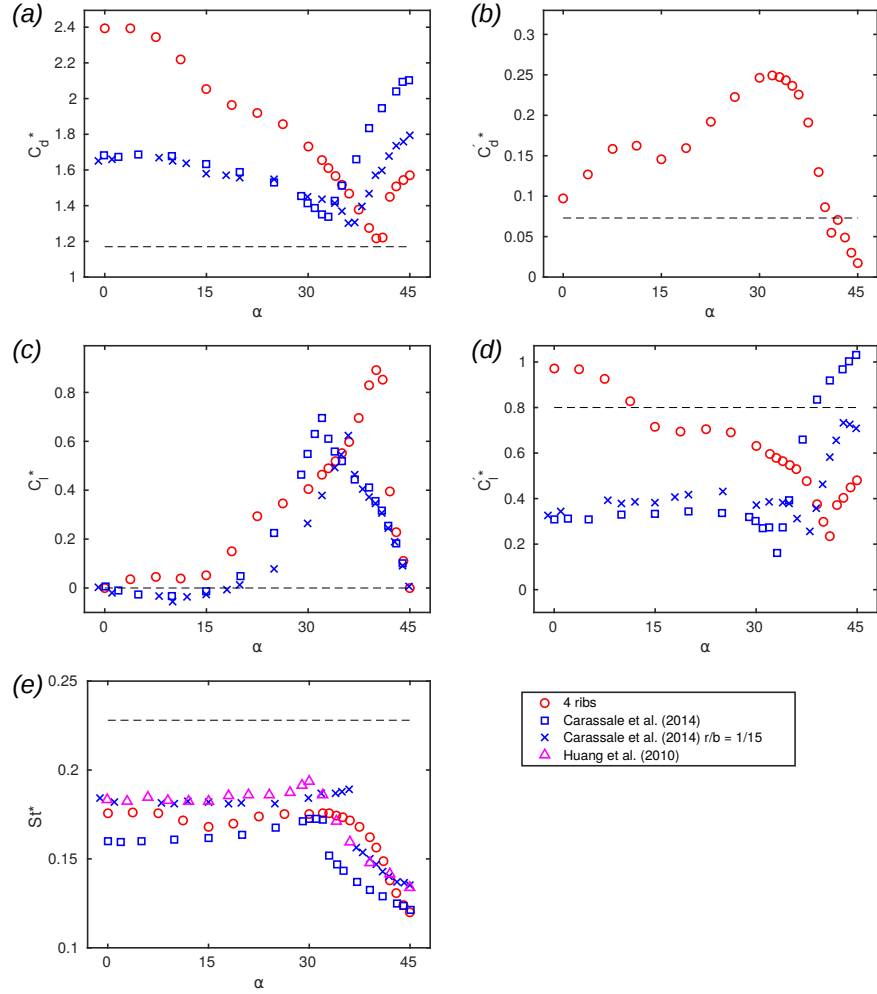
Figure 14: Mean and fluctuating lift force coefficients and Strouhal number calculated using projected frontal width as characteristic linear dimension versus angle of attack for the four-rib case and square prism: a) C_d^*, b) $C_d'^*$, c) C_l^*, d) $C_l'^*$, e) St^*. The dashed line shows the value for the smooth cylinder case. Data from Huang et al. (2010) (standard square cylinder) and Carassale et al. (2014) (standard square cylinder and square cylinder with rounded corners; datasets for smooth flow conditions) are shown for comparison where available.

the fluctuating force coefficients compared to the circular cylinder were preserved for both configurations at most angles of attack when projected frontal width was used as characteristic linear dimension. The change of characteristic linear dimension led to further reduction in Strouhal number compared to the circular cylinder. This indicates that the observed reduction of the Strouhal number is consistent with the general trend of bluff bodies with non-circular cross-section, which yield lower Strouhal number values compared to smooth, circular cylinders (Roshko, 1955).

As for the cactus-shaped cylinders, C_d^*, C_l^*, and $C_l'^*$ for the square cylinder show a strong dependence on the angle of attack (see figure 14). It should be noted that in the investigation on flow past square cylinders, a different convention for the angle of attack is used, i.e. $\alpha_{\mathrm{sq}} = 45°$ when a corner of the square is facing the flow, while in our definition this corresponds to $\alpha = 0°$, consequently $\alpha = 45° - \alpha_{\mathrm{sq}}$. In figure 14, this relationship was used to convert results from the cited studies of square cylinders to our definition of the angle of attack α.

For the square cylinder, a critical angle of attack α_{cr} is observed. At this angle of attack, the mean drag and fluctuating lift force coefficients attain their minimum and the mean lift coefficient and the Strouhal number their maximum values. This behaviour is attributed to the reattachment of the flow that separates at the front corner of the square cylinder to the back corner at this angle of attack. Similar features in the angle of attack dependence of C_d^*, C_l^*, $C_l'^*$, and St^* can be observed in the four-rib cylinder data. However, the critical angle of attack for the four-rib cylinder is higher ($\alpha_{\mathrm{cr}} \approx 40°$) compared to the value for the square cylinder, where $\alpha_{\mathrm{cr}} \approx 32°$ (Igarashi, 1984). This may be a combined effect of the corner rounding of the rib tips and of the flow within the cavities for the four-rib cylinder. Corner rounding is known to increase the critical angle for the square cylinder (Carassale et al., 2014). When comparing the four-rib cylinder results to the square cylinder with the corner rounding closest to the four-rib case ($r/b = 1/15.5$, where r is the corner radius and b is the side of the square) from Carassale et al. (2014)'s study, a stronger effect is observed in the four-rib cylinder case, even though it has a slightly smaller corner rounding radius ($r/b = 1/18.8$). In addition, the values of C_d^* and $C_l'^*$ for $\alpha > \alpha_{\mathrm{cr}}$ in the four-rib case are lower compared to those of the square with rounded corners. These differences in the angle of attack dependence compared to square cylinders with rounded corners are likely to be an effect of the cavities between the ribs, as they are the main difference in shape between the two geometries. The presence of cavities is probably also the cause of the increased values of the drag force coefficient and fluctuating lift force coefficient at lower angles of attack relative to the square cylinder. The results for the angle of attack dependence of the Strouhal number show the same trends as observed for square cylinders. At low angles of attack the Strouhal number has an approximately constant value and a decrease of St^* is observed for high angles of attack. The drop in St^* around the critical angle appears more gradual for the four-rib cylinder compared to the square, where a more sudden drop in St^* is observed.

For the three-rib cylinder, the angle-of-attack dependence of the force coefficients and Strouhal number also suggest the presence of a critical angle of attack at $\alpha_{\mathrm{cr}} \approx 27.5°$. As for the four-rib case, the minimum value of C_d^* and the maximum values of C_l^* and St^* are observed at this angle of attack. However, in contrast to the four-rib case a minimum value of $C_l'^*$ is not attained at α_{cr}, but a sudden increase is observed. Published data on the angle-of-attack dependence of the aerodynamic characteristics of equilateral triangular cylinders is limited, as most studies focus on the $0°$ and $60°$ cases. Therefore, the three-rib case is compared to experimental results for a wall-mounted, low-aspect ratio triangular prism with a free end at higher Reynolds number ($Re = 1.2 \cdot 10^5$) (Iungo and Buresti, 2009) and for a high aspect ratio triangular cylinder at lower Reynolds number ($Re = 2,700$) (Seyed-Aghazadeh et al., 2017). Due to the three-dimensionality of the former flow configuration and the large differences in Reynolds numbers no detailed quantitative comparison with the three-rib cylinder results can be made. However, the behaviour of the mean lift and drag coefficients is qualitatively consistent with the referenced results, namely the maximum of C_l^* and the minimum of C_d^* was found close to intermediate angles of attack both in the three-rib case and in the referenced studies (see figure 13 (a) and (c)).

At low angles of attack, higher values of C_d^* are observed for the three-rib cylinder compared to the triangular prism, which may be an effect of the cavities, as discussed above for the four-rib cylinder. For the Strouhal number (figure 13 e), matching trends are observed for higher angles of attack $\alpha > 27.5°$, but for low angles of attack the three-rib cylinder case shows a decreasing trend and lower St^* values than the triangular cylinder at lower Reynolds number (Seyed-Aghazadeh et al., 2017). For a more detailed comparison of the three-rib case to an equilateral triangle further comparative studies of infinitely long triangular cylinders, including cases with rounded corners, are required which are beyond the scope of the current investigation.

The minimum values of the determined aerodynamic coefficients for both configurations have been related to their angular orientation with respect to the flow. In both the three- and four-rib cases minimum values of C_d^* are observed at a critical angle of attack ($\alpha_{\mathrm{cr}} \approx 40°$ for the four-rib case and $\alpha_{\mathrm{cr}} \approx 27.5°$ for the three-rib case). At this angle of attack C_l^* reaches its maximum value for both configurations. In addition, at $\alpha \geq \alpha_{\mathrm{cr}}$ in the four-rib case relatively low values of the drag coefficient and fluctuating force coefficients are observed. Therefore, a high angle of attack $\alpha > \alpha_{\mathrm{cr}}$ relative to the prevailing wind would minimise the wind loadings experienced by the *Euphorbia Abyssinica* based cylinder as C_l^* drops off rapidly for $\alpha > \alpha_{\mathrm{cr}}$. For a three-rib cactus there is no single optimal orientation, as low C_d^* values correlate with high C_l^*. Considering the fluctuating loads on the three-rib cylinder, an angle of attack just below the critical angle may be the most favourable orientation for the *Euphorbia trigona* based cylinder, as here C_d^*, $C_l'^*$, and $C_d'^*$ all have relatively low values.

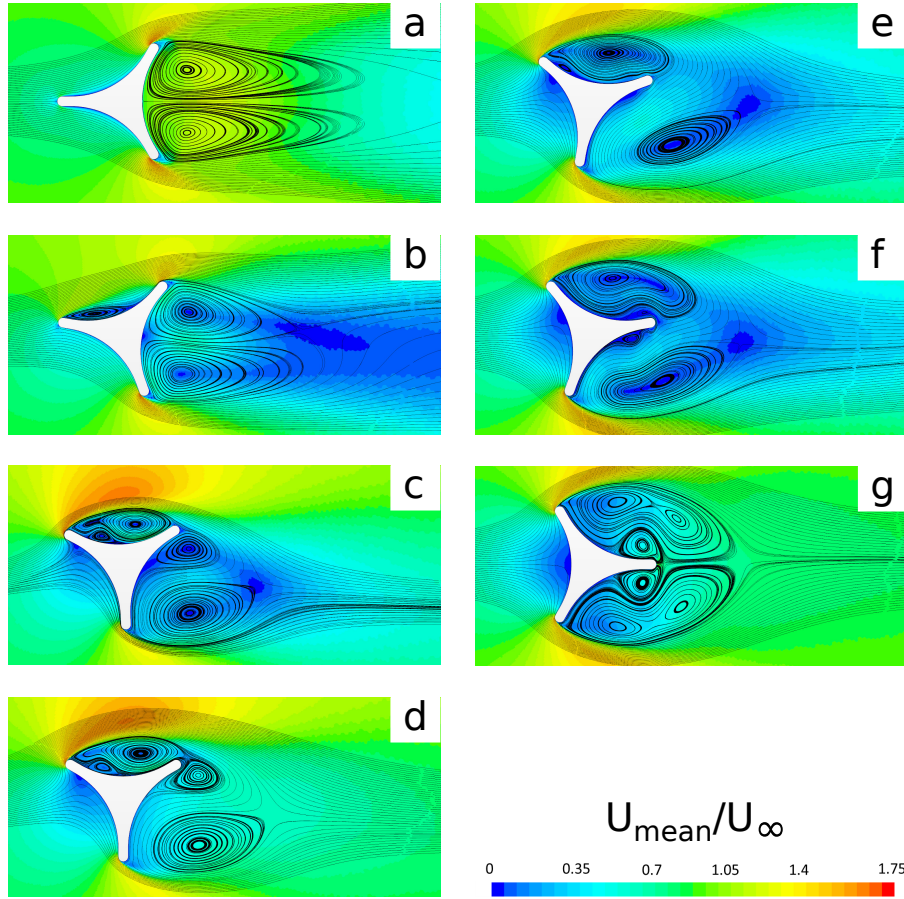Figure 15: Mean streamlines variation with angle of attack for the three-rib cylinder case: a) $\alpha = 0°$, b) $\alpha = 10°$, c) $\alpha = 27.5°$, d) $\alpha = 30°$, e) $\alpha = 40°$, f) $\alpha = 50°$, g) $\alpha = 60°$.

4.5. Flow visualisations

To gain further insight into the angle of attack dependence of the flow, in the following key features of the mean flow fields are discussed. Figure 15 shows the mean velocity field and the mean streamlines for the three-rib case at different angular orientations. At $\alpha = 0°$ the mean flow is symmetrical and two vortices are formed behind the three-rib cylinder (figure 15 a). This is consistent with experimental and numerical results by Yagmur et al. (2017) for a triangular prism at the same angular orientation. With the increase of angle of attack the symmetry is broken and an additional vortex starts to form in the top cavity (figure 15 b). At the angle $\alpha = 27.5°$ the flow detached at the front rib is still reattaches to the top trailing rib, while at $\alpha = 30°$ this is no longer observed (figure 15 c, d). The reattachment of the flow supports the conjecture regarding the critical angle of attack for the three-rib cylinder and explains minimum value of the drag coefficient and maximum value of the lift coefficient at this angle of attack. In addition, at intermediate angle of attack up to $\alpha < 50°$ a secondary vortex is observed in the top cavity (figure 15 c-e) close to the front rib. At $\alpha = 50°$ an additional vortex starts to form in the trailing bottom cavity (figure 15 f). When the cavity of the cactus shaped cylinder with three ribs is facing the flow, the symmetry of the flow is restored and in addition to the vortices formed at the top and bottom ribs smaller vortices are formed at the back rib (figure 15 g). These features are consistent with the flow visualisations of Nakagawa (1989) for the same orientation of the triangular prism.

The mean velocity field and mean streamlines for the four-rib cylinder are shown in figure 16. The mean streamlines at $\alpha = 45°$ in the four-rib case (figure 16 a) indicate the presence of recirculation zones within the cavities tangential to the flow, i.e. in the lower and the upper cavities, similar to those reported by Wang et al. (2014) and Jie and Liu (2016) for cylinders with many ribs. Deep within the cavity a secondary recirculation zone can be observed, a similar feature observed in the numerical study by Babu and Mahesh (2008) at low Re. With the decrease of the angle of attack this secondary recirculation zone in the top cavity shrinks (see figure 16 b and c) and disappears when $\alpha < 30°$. In contrast, a secondary recirculation zone in the bottom cavity is present until $\alpha = 22.5°$ (figure 16 d).

Igarashi (1984) classified the flow around a square prism into four regimes with respect to angle of attack and his classification will be used in the following. Angles of attack ranges from Igarashi (1984)'s paper given below were converted to the angle of attack definition adopted in the current paper (see also section 4.4). Visualisations with streamlines of the flow past square cylinders are given in Oka and Ishihara (2009). At $\alpha = 45°$ the flow around the square prism is characterised by a 'perfect separation' from the leading edge and by symmetric flow. The same is observed in the four-rib case at the same angle of attack (figure 16 a). However, compared to the numerical results by Oka and Ishihara (2009) the recirculation bubble in the four-rib case is significantly elongated behind the cylinder, delaying the development of a von Kármán vortex street.

For the square cylinder at angles of attack values $32° < \alpha < 40°$, the flow is characterised by a 'perfect separation' type without symmetry of the flow,
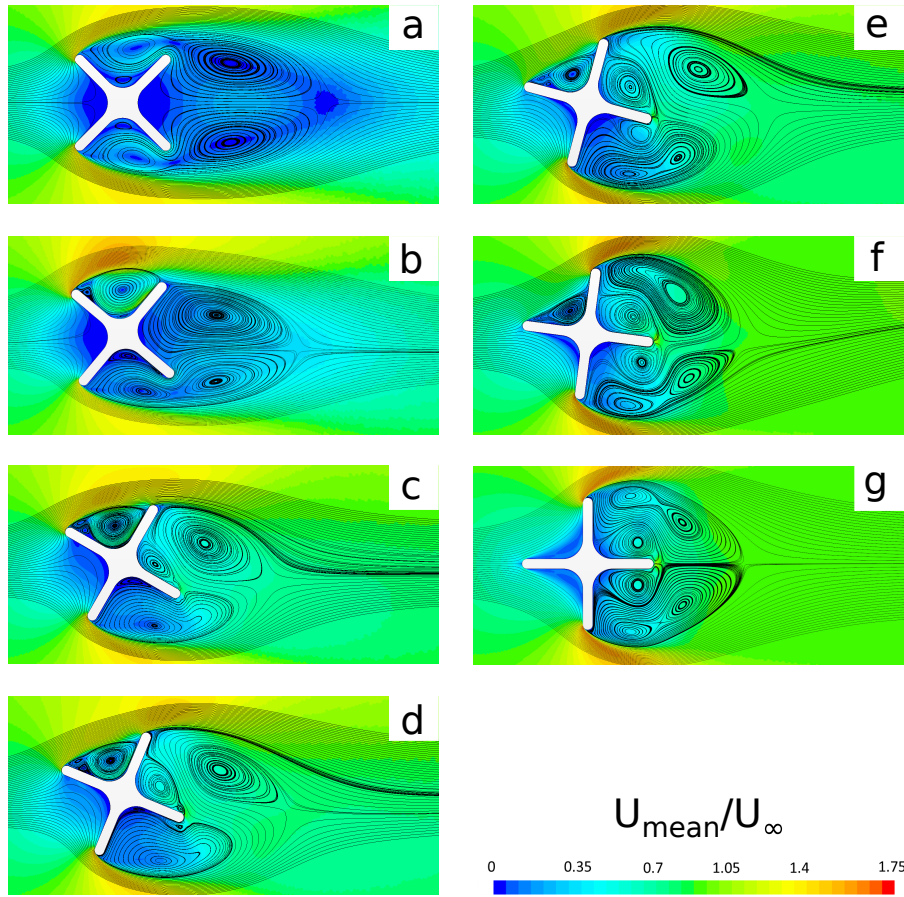
Figure 16: Mean streamlines variation with angle of attack for the four-rib cylinder case: a) $\alpha = 45°$, b) $\alpha = 40°$, c) $\alpha = 30°$, d) $\alpha = 22.5°$, e) $\alpha = 15°$, f) $\alpha = 7.5°$, g) $\alpha = 0°$.
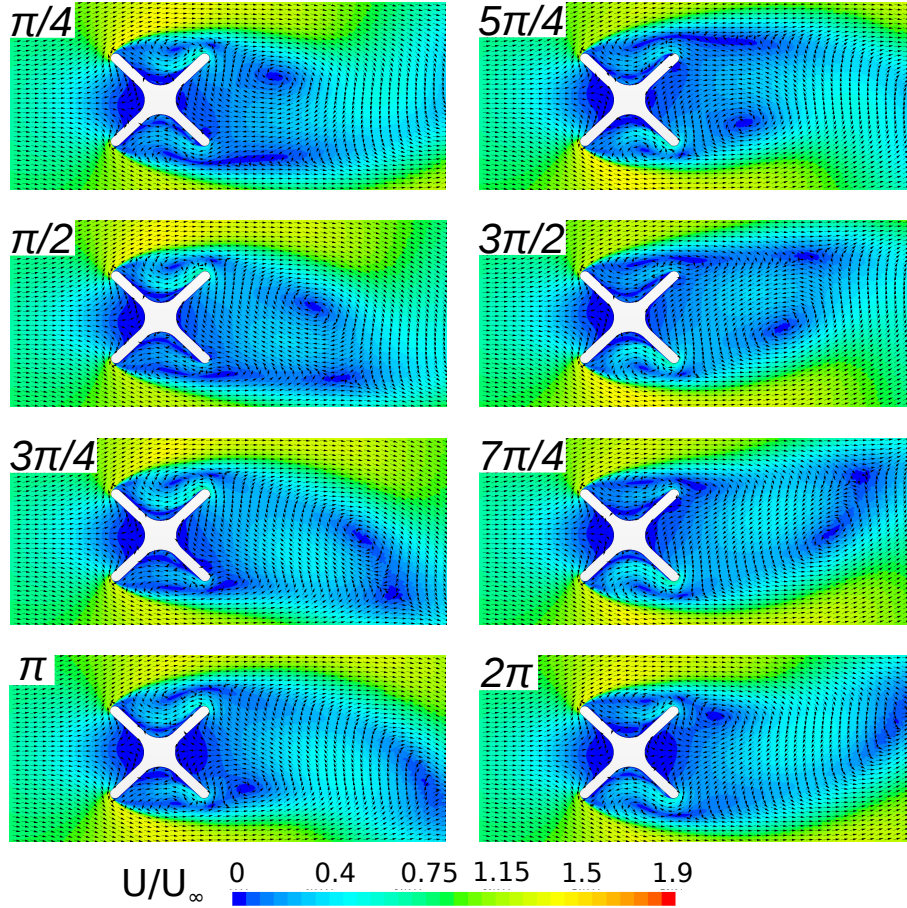
Figure 17: Vortex development around the four-rib cylinder at $\alpha = 45°$ at different phases in the shedding cycle.

while reattachment of the flow is observed in α range of $10°$ to $31°$. For the cactus-shaped cylinder with four ribs the reattachment of the flow at the back rib appears to be delayed to higher angles of attack ($\alpha = 40°$) (figure 16 b) compared to the square cylinder. This could be caused by the combined effect of the rounding of the tips of the ribs compared to the sharp corners of a classical square cylinder and the stronger development of the separated flow due the cavities. The sudden jumps in the aerodynamic coefficients and Strouhal number values in this α range are consistent with these observations (see figure 14).

To obtain further insight into the flow field variation around the four-rib cylinder, the velocity field is shown at eight different phases within the shedding cycle of the velocity field for two different angles of attack, $\alpha = 45°$ and $\alpha = 22.5°$ (see figures 17 and 18). During the formation of a new vortex in the near wake for the $\alpha = 45°$ case, this vortex interacts with the flow inside the cavity.
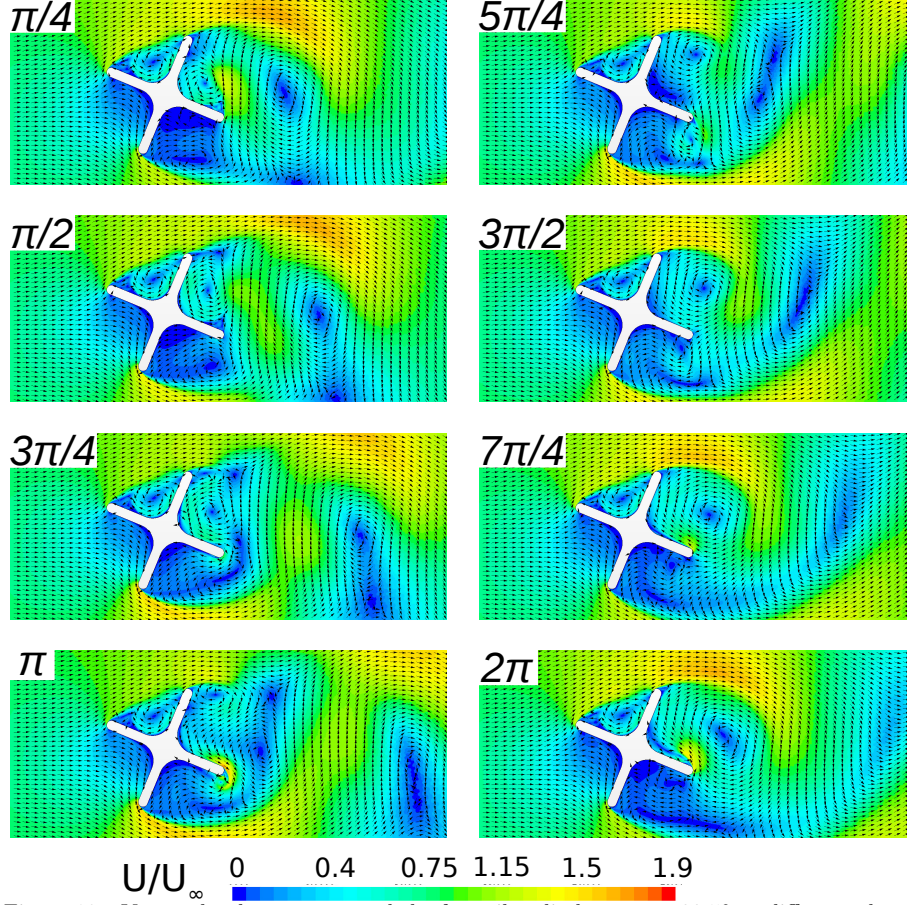
Figure 18: Vortex development around the four-rib cylinder at $\alpha = 22.5°$ at different phases in the shedding cycle.

Stronger interaction between the cavity flow and the near wake is observed than for the 24-rib cylinder due to the much wider cavities for the four-rib case. No separated flow is observed in the leading and trailing cavities. As has been discussed above, flow separation occurs at the front ribs. This is consistent with the square cylinder case where flow separates from the leading edge corners (Huang et al., 2010). In the corresponding snapshots of the velocity for $\alpha = 22.5°$ reattachment of the flow at the back ribs and asymmetric vortex shedding can be observed. For both angles of attack, the flow in the trailing cavity undergoes complete reversal as the shedding cycle progresses. High acceleration of the flow close to the back rib can be observed for the $\alpha = 22.5°$ case before this flow reversal occurs (figure 18 π and 2π). In contrast, velocity changes at the back ribs are much lower for the $\alpha = 45°$ case.

5. Conclusions

The flow past cylinders with a low number of ribs has been studied at Reynolds number 20,000 using unsteady Reynolds-Averaged Navier-Stokes simulations. Two different configurations, a three-rib configuration based on *Euphorbia trigona* and a four-rib configuration based on *Euphorbia Abyssinica*, were used for the investigation. Both shapes demonstrated strong dependence of their aerodynamic coefficients on the angle of attack. In contrast to many-rib cylinders, drag reduction was found only in the four rib case at high angles of attack.

We found that cactus-inspired cylinders with a low number of ribs can mitigate lift force fluctuations which is consistent with previous results for Saguaro-inspired cylinders with many ribs. The maximum reduction is higher, reaching up to 85% in the three-rib and up to 77% in the four-rib case compared to the smooth cylinder values. However, this is not observed over the whole angle of attack range. Reduction of the unsteady drag forces was observed only for the four-rib case at high angles of attack. Overall, the cylinder with four ribs showed at high angle of attack values of the aerodynamic coefficients superior to those at other orientations and to all tested three-rib case angular positions. In addition, it yielded mean force coefficients similar to the smooth cylinder case, while also yielding a considerable reduction of the fluctuating lift and drag coefficients. These observations remained valid when the characteristic linear dimension for calculation of the aerodynamic coefficients was changed from equivalent circle diameter to projected frontal width.

The relation between cavity orientation and minimum values of the aerodynamic coefficients shows that drag is minimised at a critical angle of attack α_{cr} while minimum lift is observed when the symmetry of the body with respect to the flow is preserved. The presence of cavities at the front and the back of the cylinder reduces unsteady drag and lift forces. This suggests that in the natural environment the orientation of the four-rib succulent stem at which aerodynamic loadings are minimised is for angles of attack higher than critical ($\alpha > \alpha_{cr} \approx 40°$). On the other hand there is no clear optimum orientation for the single stems of the three-rib succulents, although angular orientations just below the critical angle $\alpha_{cr} \approx 27.5°$ for the three-rib case appear to be the most desirable for decreasing the fluctuating loads and the mean drag.

Comparisons of the flow field around the four-rib cylinder to the square cylinder and the three-rib cylinder to triangular prisms have been performed due to their similar outer shapes. At high angles of attack the mean streamlines of the four rib-case showed features resembling the square cylinder case. However, the reattachment of the flow in the four-rib cactus-shaped cylinder case is observed at higher angle of attack compared to the square cylinder. In addition, a significant difference in flow patterns is observed at lower angles of attack, due to the more complex vortex patterns formed at cactus cylinder ribs and their interaction with vortices formed at the trailing rib.

The significant dependence of the aerodynamic characteristics on the cactus orientation with respect to the flow direction may have an effect on plants in the

real world. The stems of the succulents and cacti with a low number of ribs may be oriented relatively to the prevailing wind in order to minimise negative impact from the wind loadings, however no relevant information was found in the literature. Moreover, unlike the Saguaro cactus, which usually grows as a single stem plant with a couple of branches, succulents with a low number of ribs tend to form a bush-like structure with many branched stems. Another conjecture, which could be investigated in future work, is that the collective aerodynamic behaviour of multiple stems may have an effect similar to many-rib cylinders, consequently minimising angle of attack dependence of the aerodynamic coefficients. Previous studies of a small groups of cylinders, such as two cylinders in tandem (Alam et al., 2003b) and side-by-side arrangements (Alam et al., 2003a), as well as the investigation by Taddei et al. (2016) on large groups of cylindrical objects show that the interaction between neighbouring cylinders can have a profound effect on their aerodynamic coefficients. Therefore, we expect that interaction between multiple stems of a succulent will influence the force coefficients experienced by the individual stems as well as the plant as the whole.

References

Abboud, J.E., Karaki, W.S., Oweis, G.F., 2011. Particle image velocimetry measurements in the wake of a cactus-shaped cylinder. Journal of Fluids Engineering 133, 094502. doi:10.1115/1.4004824.

Alam, M.M., Moriya, M., Sakamoto, H., 2003a. Aerodynamic characteristics of two side-by-side circular cylinders and application of wavelet analysis on the switching phenomenon. Journal of Fluids and Structures 18, 325–346. doi:10.1016/j.jfluidstructs.2003.07.005.

Alam, M.M., Moriya, M., Takai, K., Sakamoto, H., 2003b. Fluctuating fluid forces acting on two circular cylinders in a tandem arrangement at a subcritical Reynolds number. Journal of Wind Engineering and Industrial Aerodynamics 91, 139–154. doi:10.1016/S0167-6105(02)00341-0.

Apaçoğlu, B., Aradağ, S., 2011. CFD analysis of uncontrolled and controlled turbulent flow over a circular cylinder, in: 6th International Advanced Technologies Symposium (IATS'11), pp. 60–65.

Babu, P., Mahesh, K., 2008. Aerodynamic loads on cactus-shaped cylinders at low Reynolds numbers. Physics of Fluids 20, 035112. doi:10.1063/1.2887982.

Benim, A., Pasqualotto, E., Suh, S., 2008. Modelling turbulent flow past a circular cylinder by RANS, URANS, LES and DES. Progress in Computational Fluid Dynamics, an International Journal 8, 299–307. doi:10.1504/PCFD.2008.019483.

Carassale, L., Freda, A., Marrè-Brunenghi, M., 2014. Experimental investigation on the aerodynamic behavior of square cylinders with

rounded corners. Journal of Fluids and Structures 44, 195–204. doi:10.1016/j.jfluidstructs.2013.10.010.

El-Makdah, A.M., Oweis, G.F., 2013. The flow past a cactus-inspired grooved cylinder. Experiments in Fluids 54, 1464. doi:10.1007/s00348-013-1464-z.

Huang, R., Lin, B., Yen, S., 2010. Time-averaged topological flow patterns and their influence on vortex shedding of a square cylinder in crossflow at incidence. Journal of Fluids and Structures 26, 406–429. doi:10.1016/j.jfluidstructs.2010.01.003.

Igarashi, T., 1984. Characteristics of the flow around a square prism. Bulletin of JSME 27, 1858–1865. doi:10.1299/jsme1958.27.1858.

Iungo, G.V., Buresti, G., 2009. Experimental investigation on the aerodynamic loads and wake flow features of low aspect-ratio triangular prisms at different wind directions. Journal of Fluids and Structures 25, 1119–1135. doi:10.1016/j.jfluidstructs.2009.06.004.

Jie, H., Liu, Y.Z., 2016. Large eddy simulation of turbulent flow over a cactus-analogue grooved cylinder. Journal of Visualization 19, 61–78. doi:10.1007/s12650-015-0294-x.

Ju, J., Bai, H., Zheng, Y., Zhao, T., Fang, R., Jiang, L., 2012. A multi-structural and multi-functional integrated fog collection system in cactus. Nature communications 3, 1247. doi:10.1038/ncomms2253.

Letchford, C., Lander, D., Case, P., Dyson, A., Amitay, M., 2016. Bio-mimicry inspired tall buildings: The response of cactus-like buildings to wind action at Reynolds number of 10^4. Journal of Wind Engineering and Industrial Aerodynamics 150, 22–30. doi:10.1016/j.jweia.2016.01.001.

Lim, H.C., Lee, S.J., 2002. Flow control of circular cylinders with longitudinal grooved surfaces. AIAA Journal 40, 2027–2036. doi:10.2514/2.1535.

Liu, Y.Z., Shi, L.L., Yu, J., 2011. TR-PIV measurement of the wake behind a grooved cylinder at low Reynolds number. Journal of Fluids and Structures 27, 394–407. doi:10.1016/j.jfluidstructs.2010.11.013.

Lysenko, D.A., Ertesvåg, I.S., Rian, K.E., 2014. Large-eddy simulation of the flow over a circular cylinder at Reynolds number 2×10^4. Flow, Turbulence and Combustion 92, 673–698. doi:10.1007/s10494-012-9405-0.

McGhee, G.R., 2011. Convergent evolution: limited forms most beautiful. MIT Press. doi:10.7551/mitpress/9780262016421.001.0001.

Nakagawa, T., 1989. Vortex shedding mechanism from a triangular prism in a subsonic flow. Fluid dynamics research 5, 69–81. doi:10.1016/0169-5983(89)90012-9.

27

Norberg, C., 2003. Fluctuating lift on a circular cylinder: review and new measurements. Journal of Fluids and Structures 17, 57–96. doi:10.1016/S0889-9746(02)00099-3.

Oka, S., Ishihara, T., 2009. Numerical study of aerodynamic characteristics of a square prism in a uniform flow. Journal of Wind Engineering and Industrial Aerodynamics 97, 548–559. doi:10.1016/j.jweia.2009.08.006.

Pierson, E.A., Turner, R.M., 1998. An 85-year study of saguaro (Carnegiea gigantea) demography. Ecology 79, 2676–2693. doi:10.1890/0012-9658(1998)079[2676:AYSOSC]2.0.CO;2.

Roshko, A., 1955. On the wake and drag of bluff bodies. Journal of the Aeronautical Sciences 22, 124–132. doi:10.2514/8.3286.

Seyed-Aghazadeh, B., Carlson, D.W., Modarres-Sadeghi, Y., 2017. Vortex-induced vibration and galloping of prisms with triangular cross-sections. Journal of Fluid Mechanics 817, 590–618. doi:10.1017/jfm.2017.119.

Siemens, 2017. Star-CCM+. URL: http://http://mdx.plm.automation.siemens.com/. accessed: 2017-05-15.

Taddei, S., Manes, C., Ganapathisubramani, B., 2016. Characterisation of drag and wake properties of canopy patches immersed in turbulent boundary layers. Journal of Fluid Mechanics 798, 27–49. doi:10.1017/jfm.2016.312.

Talley, S., Iaccarino, G., Mungal, G., Mansour, N., 2001. An experimental and computational investigation of flow past cacti. Annual Research Briefs, Center for Turbulence Research, NASA Ames/Stanford University , 51–63.

Talley, S., Mungal, G., 2002. Flow around cactus-shaped cylinders. Center for Turbulence Research, Annual Research Briefs 2002, 363–376.

Teboho, N., Mpholo, M., Lennard, C., 2017. Long-term austral summer wind speed trends over southern Africa. International Journal of Climatology 37, 2850–2862. doi:10.1002/joc.4883.

Wang, S.F., Liu, Y.Z., Zhang, Q.S., 2014. Measurement of flow around a cactus-analogue grooved cylinder at $Re_d = 5.4 \times 10^4$: Wall-pressure fluctuations and flow pattern. Journal of Fluids and Structures 50, 120–136. doi:10.1016/j.jfluidstructs.2014.06.019.

West, G., Apelt, C., 1993. Measurements of fluctuating pressures and forces on a circular cylinder in the Reynolds number range 10^4 to 2.5×10^5. Journal of Fluids and Structures 7, 227–244. doi:10.1006/jfls.1993.1014.

Yagmur, S., Dogan, S., Aksoy, M.H., Goktepeli, I., Ozgoren, M., 2017. Comparison of flow characteristics around an equilateral triangular cylinder via PIV and Large Eddy Simulation methods. Flow Measurement and Instrumentation 55, 23–36. doi:10.1016/j.flowmeasinst.2017.04.001.

Yamagishi, Y., Oki, M., 2004. Effect of groove shape on flow characteristics around a circular cylinder with grooves. Journal of Visualization 7, 209–216. doi:10.1007/BF03181635.

Yamagishi, Y., Oki, M., 2005. Effect of the number of grooves on flow characteristics around a circular cylinder with triangular grooves. Journal of Visualization 8, 57–64. doi:10.1007/BF03181603.

Zhou, B., Wang, X., Guo, W., Zheng, J., Tan, S.K., 2015. Experimental measurements of the drag force and the near-wake flow patterns of a longitudinally grooved cylinder. Journal of Wind Engineering and Industrial Aerodynamics 145, 30–41. doi:10.1016/j.jweia.2015.05.013.